

## MODELS FOR SOLAR MAGNETIC LOOPS. III. DYNAMIC MODELS AND CORONAL DIAGNOSTIC SPECTROMETER OBSERVATIONS

E. LANDI

Artep, Inc., Ellicott City, MD 21042; and Naval Research Laboratory, Space Science Division,  
4555 Overlook Avenue SW, Code 7600A, Washington, DC 20375-5320

AND

M. LANDINI

Università degli Studi di Firenze, Largo Enrico Fermi 2, 50125 Florence, Italy

Received 2003 December 1; accepted 2004 March 3

### ABSTRACT

In the present work *SOHO* Coronal Diagnostic Spectrometer (CDS) observations of a quiescent active region loop are compared to a steady state, dynamic loop model. Three different heating functions are adopted: uniform, concentrated at the top, and concentrated at the footpoints. Predicted temperature and density profiles of the selected loop are compared with those obtained from CDS observations using line ratios and an emission measure analysis. The latter method also allows us to measure the loop filling factor. The space of parameters of the model is investigated in an effort to achieve agreement with observations. The effects of uncertainties and of CDS instrumental limitations on the results are assessed. We find that no agreement can be found between model predictions and observations. Possible causes of the disagreement and areas of further investigation are discussed. This work also demonstrates the potential of high-resolution spectroscopy in loop studies, even in the presence of moderate spatial resolution.

*Subject headings:* plasmas — Sun: corona — Sun: magnetic fields

### 1. INTRODUCTION

Results from imaging instruments working at X-ray, ultraviolet, and extreme-ultraviolet (EUV) wavelengths have shown that plasma loops are a fundamental component for both the quiet and active solar corona. Therefore, their understanding is an essential step required for an accurate knowledge of the structure of the solar atmosphere, as well as for unveiling the elusive mechanism(s) that heat the solar corona. Narrowband imagers and spectrometers on board the *Yohkoh*, *SOHO*, and *TRACE* satellites have provided a wealth of observations of loops that brought a renewed interest in loop physics.

Narrowband images from *TRACE* and the EUV Imaging Telescope (EIT) on *SOHO* and broadband images from *Yohkoh* have allowed us to investigate loops with a far greater spatial resolution than in most previous missions and with unparalleled cadence. The high spatial resolution and cadence, as well as the continuous observation of the Sun in selected spectral bands, have made it possible to identify a large number of individual loop structures and to follow their evolution with time. However, such observations have left us with a very confused understanding of coronal loops and their heating, since inadequate temperature resolution and coverage have been fundamental limitations. Even the most basic questions are still unanswered.

Temperature diagnostics using filter ratios from *SOHO* EIT, *TRACE*, and the Soft X-Ray Telescope (SXT) on board *Yohkoh* have allowed several authors (Neupert et al. 1998; Aschwanden et al. 1999, 2000; Lenz et al. 1999; Priest et al. 1998, 2000) to investigate the plasma temperature profile along several loops. Observed temperature profiles are much more constant than predicted by standard theoretical models such as the Rosner et al. (1978) model. These results led Aschwanden et al. (1999, 2000) to state that coronal loops with temperatures in

the range  $(1-2.5) \times 10^6$  K are not under steady state conditions. However, inadequate spatial resolution can cause the mixing of different subresolution filaments within each pixel, leading to a fake isothermality. In fact, Reale & Peres (2000) suggested that the very small temperature gradient could be due to the presence of filamentation. They reproduced the observed temperature profiles using several unresolved standard loops at different temperatures. A similar approach has been adopted by Warren et al. (2002), using a time-dependent hydrodynamical code. However, narrowband imagers are affected by two main limitations. Filter ratio techniques, when applied to narrowband photometry, have limited validity (e.g., Testa et al. 2002; Martens et al. 2002), and more accurate results can only be obtained by spectrometers. Moreover, imagers are unable to provide filling factor measurements necessary to confirm the presence of filamentation. Filling factors can only be obtained through the use of spectrometers.

Imager-related studies have failed to provide a coherent picture on loop heating. For example, soft X-ray loops observed by *Yohkoh* have been shown to be equally compatible with two completely different coronal heating scenarios: one with perfectly steady and uniform heating (Klimchuk & Porter 1995) and the other with nanoflares occurring randomly in thousands of subresolution strands (Cargill & Klimchuk 1997). In another example of a particularly well studied *Yohkoh* loop, the heating was variously found to be uniform (Priest et al. 2000), concentrated near the footpoints (Aschwanden 2001), and concentrated near the apex (Reale 2002). Ambiguities are also present in the interpretation of *TRACE* data (Testa et al. 2002; Chae et al. 2002), again because of the limited temperature diagnostic capability of narrowband imagers. By studying the temperature distribution of the plasma in loops observed with the Coronal Diagnostic Spectrometer (CDS), Martens et al. (2002) suggested that the heating was concentrated at

the loop top. In general, no definitive results on the nature and location of loop heating have been obtained.

By comparing *TRACE* observations of 67 loops with a static, steadily heated loop model, Winebarger et al. (2003) have shown that static loop models are poor representations of most active region loops and that dynamics needs to be included. However, velocity measurements can only be obtained by spectrometers.

Detailed measurements of plasma properties along loops using monochromatic images and line ratio techniques are surprisingly scarce, despite the great opportunities given by the two *SOHO* spectrographs CDS and SUMER. Most of the attention has been focused on velocity studies in active region loops. For example, Winebarger et al. (2002) measured velocities up to 40 km s<sup>-1</sup> in active region loops observed by SUMER.

Until recently, little attention has been paid to density, temperature, abundance, and filling factor measurements from spectra, despite the fact that emission-line spectra provide a much higher temperature resolution than imagers and allow us to measure plasma parameters much more precisely than narrowband images from EIT, *Yohkoh*, and *TRACE*. The limiting factors that have prevented an extensive use of the *SOHO* spectrometers for loop studies have been their inadequate spatial and temporal resolution.

The only attempts have been made by Dr. J. T. Schmelz and coworkers (Schmelz et al. 2001; Schmelz 2002; Martens et al. 2002), Brković et al. (2002, hereafter Paper I), and Di Giorgio et al. (2003) using CDS observations of active region loops at the limb or the disk. Schmelz et al. (2001) find contradictory results from an active region at the limb: while line intensity ratios pointed toward a constant temperature along the loop, a differential emission measure (DEM) analysis showed a multithermal behavior across the loop section. Different results have been found in Paper I, where an emission measure (EM) analysis was used to show that the loop plasma is isothermal both along and across the loop shape, thus putting into question the presence of multithermal subresolution filaments. Di Giorgio et al. (2003) analyzed time-resolved CDS and *Yohkoh* observations of an active region loop, detecting moderate activity; they propose several scenarios that might account for it but conclude that higher spatial and temporal resolution is needed. Paper I showed that uniform heating was inadequate in a static loop scenario and proposed footpoint-concentrated heating as a possible solution. Martens et al. (2002), on the contrary, suggested heating concentrated at the top as an explanation for multithermal structure in CDS loops.

The aim of the present paper is to compare a one-dimensional, steady state, dynamic loop model with CDS observations of a quiescent active region loop. After determining the loop shape and subtracting the background emission, we measure the main physical properties of the loop: electron temperature, density, EM, filling factor, and plasma velocities. The electron temperature is determined by two different techniques. We compare the resulting density and temperature profiles along the loop with predictions from the theoretical model, calculated by adopting the three functional forms for the heating function most used in recent studies: uniform, concentrated at the top, and concentrated at the footpoints. The comparison shows that none of the proposed heating reproduces the observations. The importance of observational uncertainties and possible areas of further investigation are proposed. As a by-product, the present work demonstrates that even with its moderate spatial resolution, CDS can provide important measurements

of loop physical parameters and stringent constraints on loop models and heating.

In § 2 we introduce the theoretical model that will be compared to the CDS observations, described in § 3. In § 4 the loop physical properties are measured along the loop length and across its cross section. In § 5 we report the comparison of the measured density and temperature profiles with predictions, discuss the three different heating functions adopted and the effects of observational uncertainties in the input parameters of the model, and suggest a few possible scenarios that might account for the results of the comparison. In § 6 we summarize the results of the whole work.

## 2. THEORETICAL MODEL

The loop model we consider in the present work is an update of the model first developed by Landini & Monsignori Fossi (1981, hereafter LM81) and consists of a one-dimensional, stationary, nonstatic model where velocities are nonnegligible and subsonic everywhere in the loop, so that shocks cannot develop at any point. The loop is also assumed to be toroidal and with constant cross section.

The model solves the equation of state, along with the equations of conservation of mass, momentum, and energy, respectively, which can be expressed in the following form:

$$p = \frac{R}{\mu} \rho T, \quad (1)$$

$$\rho v = \text{constant}, \quad (2)$$

$$v \frac{dv}{dz} = -g_{\parallel} - \frac{1}{\rho} \frac{dp}{dz}, \quad (3)$$

$$\rho v \left[ \frac{d}{dz} \left( \frac{v^2}{2} + \frac{RT\gamma}{\gamma+1} \right) + g_{\parallel} \right] + \rho \dot{Q} = 0, \quad (4)$$

where  $z$  is the distance along the loop,  $\mu$  ( $=0.62$ ; from Priest 1982, p. 82) is the mean particle mass,  $R = 8.31 \times 10^7$  ergs mol<sup>-1</sup> K<sup>-1</sup>,  $\gamma = 5/3$ , and  $g_{\parallel}$  is the solar gravity acceleration along the loop axis, given by

$$g_{\parallel} = g \cos \theta \cos \alpha, \quad (5)$$

where  $g$  is the solar gravity acceleration,  $\theta$  is the angle at the center of the loop's torus corresponding to position  $z$ , and  $\alpha$  is the inclination of the loop's plane relative to the normal direction. In the present work we generalize the LM81 model by modifying the energy equation in order to introduce a generic heating term, given by  $E_i(T)$ , and a more accurate calculation of the radiative energy losses  $\epsilon(T)$ , calculated using the CHIANTI database (Dere et al. 1997; Young et al. 2003).

The energy term  $\rho \dot{Q}$  includes the energy lost by the loop through radiation ( $E_{\text{rad}}$ ), the energy transported through conduction ( $E_c$ ), and the energy input to the loop ( $E_i$ ):

$$\rho \dot{Q} = E_c + E_i - E_{\text{rad}}. \quad (6)$$

The energy lost by radiation is expressed by using the radiative losses function  $\epsilon(T)$  calculated using the CHIANTI database:

$$E_{\text{rad}} = C \rho^2 \epsilon(T) = C \rho^2 \frac{\eta(T)}{T^{1/2}}, \quad (7)$$

where the constant  $C = 2.55 \times 10^{47} \text{ g}^{-2}$ , and  $\eta(T)$  represents the total plasma emissivity scaled by  $T^{1/2}$ . The conductive energy is given, in the one-dimensional case, by

$$E_c = -\frac{dF_c}{dz} F_c = -AT^{5/2} \frac{dT}{dz}, \quad (8)$$

where  $F_c$  is the conductive flux and  $A = 0.92 \times 10^{-6} \text{ ergs cm}^{-1} \text{ s}^{-1} \text{ K}^{-7/2}$  (Spitzer 1962, p. 144). The input energy is assumed to be dependent on  $z$ , using the form

$$E_i = E_i^0 H(z). \quad (9)$$

The function  $H(z)$  can be chosen by the user.

In order to solve the equations of the model, we parameterize the plasma temperature, density, and velocity of the loop in order to obtain dimensionless equations, along the guidelines of LM81. We define the scaled quantities  $t$ ,  $\rho'$ , and  $x$  as

$$T = tT_M, \quad (10)$$

$$\rho = \rho' \rho_M, \quad (11)$$

$$V = xv_M = x\sqrt{aRT_M}, \quad (12)$$

where  $T_M$ ,  $\rho_M$ , and  $v_M$  are the values of plasma temperature, density, and velocity at point  $M$ , defined as the point where  $z(M)$  is equal to the loop's torus radius  $R_{\text{loop}}$ . Using this parameterization, equations (1)–(4) can be expressed in the scaled quantities and put as a function of only three quantities: scaled temperature  $t$ , scaled density  $\rho'$ , and scaled conductive flux  $f$ , all functions of the angle  $\theta$  correspondent to the distance  $z$  along the loop:

$$\theta = \frac{z}{R_{\text{loop}}}, \quad (13)$$

$$p' = \frac{t}{x}, \quad (14)$$

$$x\rho' = 1, \quad (15)$$

$$\frac{dt}{d\theta} = -\frac{f}{t^{5/2}}, \quad (16)$$

$$\frac{d\rho'}{d\theta} = \frac{\rho'}{t^{5/2}} \frac{F_0 t^{5/2} - f}{a - \rho'^2 t}, \quad (17)$$

$$\begin{aligned} \frac{df}{d\theta} = & \frac{G_0 a^{1/2}}{t^{5/2}} \left( t\rho'^2 \frac{F_0 t^{5/2} - f}{a - \rho'^2 t} + \frac{f}{\gamma + 1} \right) \\ & + \frac{T_M^{1/2}}{\rho_M^2} E_i(\theta) - C \frac{\rho'^2}{t^{1/2}} \epsilon(t) \end{aligned} \quad (18)$$

(eqs. [14]–[18] refer to the equation of state, mass, conductive flux, momentum, and energy, respectively), where

$$\begin{aligned} F_0 = & \frac{\sqrt{A} T_M}{R} \frac{GM_\odot}{\rho_M (R_\odot + R_{\text{loop}} \sin \theta)^2} \cos \theta \cos \alpha \\ G_0 = & \sqrt{\frac{R^3}{A}}, \end{aligned} \quad (19)$$

where  $\alpha$  is the inclination of the loop's plane relative to the normal direction. The quantities  $t$ ,  $\rho'$ ,  $x$ ,  $p'$ ,  $\theta$ , and  $f$  are the

plasma temperature, density, velocity, pressure, position along the loop, and conductive flux as defined by equations (10)–(12) and by

$$p = p' p_M, \quad \text{with } p_M = R \rho_M T_M, \quad (20)$$

$$F_c = f F_M, \quad \text{with } F_M = \sqrt{A} \rho_M T_M^{3/2}, \quad (21)$$

$$\theta = zh_M, \quad \text{with } h_M = \sqrt{A} \frac{T_M^2}{\rho_M} = R_{\text{loop}}. \quad (22)$$

By imposing that the  $h_M$  be equal to the loop radius  $R_{\text{loop}}$ , equations (15)–(18) can be solved using the scaled length  $\theta$ , and the integration is carried out for  $\theta = 0$  to  $\theta = \pi$ . The numerical integration is performed with a variable space grid, determined imposing that the difference in temperature and radiated energy between two adjacent grid points be smaller than 10% and 1%, respectively.

The temperature of both loop footpoints is arbitrarily chosen to be  $10^4 \text{ K}$ . The input parameters are as follows:

1. The plasma pressure  $p_0$  at the footpoint with  $\theta = 0$  (from observations).
2. The total loop length  $L_{\text{loop}}$  (from observations).
3. The inclination  $\alpha$  of the loop plane relative to the vertical (from observations).
4. The conductive flux at the footpoints  $F_0$  (chosen by the user).
5. The velocity parameter  $a$  (chosen by the user).
6. The shape of the energy input  $H(z)$  (chosen by the user).

Once these values are defined, the loop model is completely defined.

The use of  $L_{\text{loop}}$ ,  $p_0$ , and  $\alpha$  as input parameters derived from the observations represents an improvement over the LM81 model. In fact, once they are specified, the density and gravity effects are determined, so that the radiative losses and the energy balance depend only on  $a$ ,  $F_0$ , and  $H(z)$ . Therefore, once these three parameters are selected by the user, the amplitude of the heating  $E_i^0$  is also fixed and can be evaluated by using an iterative procedure that determines the value of  $E_i^0$  that allows the temperature of the right-hand footpoint ( $\theta = \pi$ ) to be  $10^4 \text{ K}$ .

The advantage of this approach is to fully exploit the observations to constrain the loop model, by limiting to  $a$ ,  $F_0$ , and  $H(z)$  the free parameters, whose space can be easily explored.

### 3. OBSERVATIONS

The observations were recorded on 1997 April 29 with CDS (Harrison et al. 1995), EIT (Delaboudinière et al. 1995), the Michelson Doppler Interferometer (MDI; Scherrer et al. 1995), and SXT (Tsuneta et al. 1991) on *Yohkoh*. A more complete description of these observations and the data reduction is given in Paper I, which also used the same observations for a comparison with an earlier and more limited version of the present model. Here we only provide a brief outline.

The CDS observations have been carried out using the  $2'' \times 240''$  slit on the Normal Incidence Spectrometer (NIS). The CDS slit scanned an active region on the solar disk centered at around  $(-100'', -400'')$ , with  $2''.03$  steps along the solar east-west direction. The size of the field of view was  $243''.6 \times 240''.2$ . The exposure time for each slit position was 60 s.

TABLE 1  
LINES OBSERVED WITH CDS AND USED IN THE ANALYSIS

Line	log $T$	Detector
Si VIII $\lambda$ 314.327*.....	5.93	NIS 1
Mg VIII $\lambda$ 315.039.....	5.91	NIS 1
Fe XIII $\lambda$ 318.128*.....	6.20	NIS 1
Fe XIV $\lambda$ 334.172*.....	6.27	NIS 1
Fe XVI $\lambda$ 335.410.....	6.43	NIS 1
Fe XII $\lambda$ 338.278*.....	6.14	NIS 1
Fe XIII $\lambda$ 348.183*.....	6.20	NIS 1
Ne V $\lambda$ 359.382.....	5.47	NIS 1
Fe XIII $\lambda$ 359.642*.....	6.20	NIS 1
Fe XIII $\lambda$ 359.842*.....	6.20	NIS 1
Fe XVI $\lambda$ 360.760.....	6.43	NIS 1
Fe XII $\lambda$ 364.467*.....	6.14	NIS 1
Mg VII $\lambda$ 367.674.....	5.81	NIS 1
Mg VII $\lambda$ 367.683.....	5.81	NIS 1
Mg IX $\lambda$ 368.070.....	5.98	NIS 1
Si XII $\lambda$ 520.665.....	6.27	NIS 2
Si XI $\lambda$ 580.907.....	6.20	NIS 2
He I $\lambda$ 584.334.....	4.00	NIS 2
O III $\lambda$ 599.597.....	4.96	NIS 2
Si XI $\lambda$ 604.147.....	6.20	NIS 2
O V $\lambda$ 629.730.....	5.39	NIS 2

NOTE.—An asterisk denotes density-dependent lines.

In order to maintain the high cadence of the observations, 16 spectral windows were extracted, containing a total of 19 spectral lines of interest for our analysis. These lines are listed in Table 1, together with estimates of their formation temperatures; they allow us to sample plasma from the chromosphere, the transition region, and the corona. The selected lines allow the electron density to be measured using pairs of Fe XII and Fe XIII lines. The presence of consecutive stages of ionization for several elements allows temperature diagnostics through flux ratios of lines of different ions of the same element. EIT, SXT, and MDI observations were taken within 2 hr from the CDS scan.

CDS raw data were cleaned and calibrated, and cosmic rays were removed by using the standard routines and calibration data available in the CDS software tree. EIT, *Yohkoh*, and MDI data were co-aligned to the CDS field of view taking into account the different pixel size and allowing for the moderate nonsimultaneity with the CDS scans.

In Paper I, by using time series of EIT observations in the  $\lambda$ 195 channel, we showed that the active region and its loops were quiescent for the duration of the observations.

### 3.1. Loop Selection

Images of the field of view from MDI, *Yohkoh*, EIT, and CDS are displayed in Figures 1 and 2. Monochromatic images from CDS were obtained by measuring the total flux under each line's profile, minus the background, in each spatial pixel. A few loops are visible in the field of view, although the moderate spatial resolution of CDS does not allow us to resolve them completely from nearby structures. Plasma at different temperatures is confined in different plasma structures, as shown, for example, by Mg IX and Fe XVI. The loop shape selected for the present work is displayed in Figure 3, where CDS and EIT observations are combined to enhance the loop left footpoint. Figures 1, 2, and 3 clearly show that the CDS spatial resolution is inadequate to properly resolve plasma loops. Spectrometers with higher spatial resolution are

greatly needed in order to enhance the loop shape selection and improve loop diagnostic studies. However, in the remainder of the present work we show that despite this huge limitation, meaningful loop diagnostics can still be made with these data. Figure 3 shows that the left footpoint is rather well defined by EIT, but residual uncertainties on the location of the right footpoint are still present. Their effects on the comparison with the loop model are discussed in § 5.

The emission in the selected loop shape has been divided into 21 subsections of approximately the same length along the loop. Spectra have been summed in each subsection, and a Gaussian spectral line shape has been fitted to each line. It is important to note that the loop shape and the choice of the subsections are different from those in Paper I: this change allowed a more accurate background subtraction. In addition, since the CDS slit rastered the field of view along the east-west direction, the subsections' data are not simultaneous.

### 3.2. Background Subtraction

In order to analyze only the true emission from the loop, we have subtracted the “ambient” background radiation. The choice of the background is crucial, especially when dealing with instruments with moderate spatial resolution like CDS, since the presence of any structures close to the selected loop contaminates its emission. In the present work, the background to be subtracted to each subsection has been determined by averaging the emission of the pixels adjacent to each subsection, in a similar way as described in Paper I. This choice has allowed us to take into account the variation of the background emission along the loop shape.

Background-subtracted intensities for a selection of lines are displayed in Figure 4, which shows that after subtraction, the intensities of all the lines emitted by the chromosphere and the transition region oscillate around zero: they are composed by background radiation only. The hottest coronal lines have nonzero, smoothly varying intensities along the whole structure (i.e., Si XI, Si XII, Fe XII, Fe XIII, Fe XIV, Fe XVI). Only these lines can be considered to be truly emitted by the loop and are considered in the rest of this work.

It is interesting to note that the intensities of coronal lines in the two subsections at around 3–40,000 km are higher than the rest of the loop. This can be due either to some activity in the loop structure, similar to the one discussed by Di Giorgio et al. (2003), or to some residual background contamination. The second scenario seems to be ruled out by the analysis in the next section. Unfortunately, the possibility of small-scale activity cannot be tested, as a result of the poor time resolution of CDS, which confirms the need for new, higher cadence spectrometers.

## 4. PLASMA DIAGNOSTICS

The electron density was measured using Fe XIII line flux ratios, preferred over Fe XII ratios, which were shown to have problems by Binello et al. (2001). An example of Fe XIII density measurement is shown in Figure 5. The line ratio method is described by Mariska (1992), where also several applications are described. The electron temperature was measured using two different methods: line flux ratios between lines of different Fe ions, and using an EM analysis, described in § 4.1. The latter method also provided a measurement of the EM of the plasma. The use of two different techniques for temperature diagnostics also allowed us to check the reliability

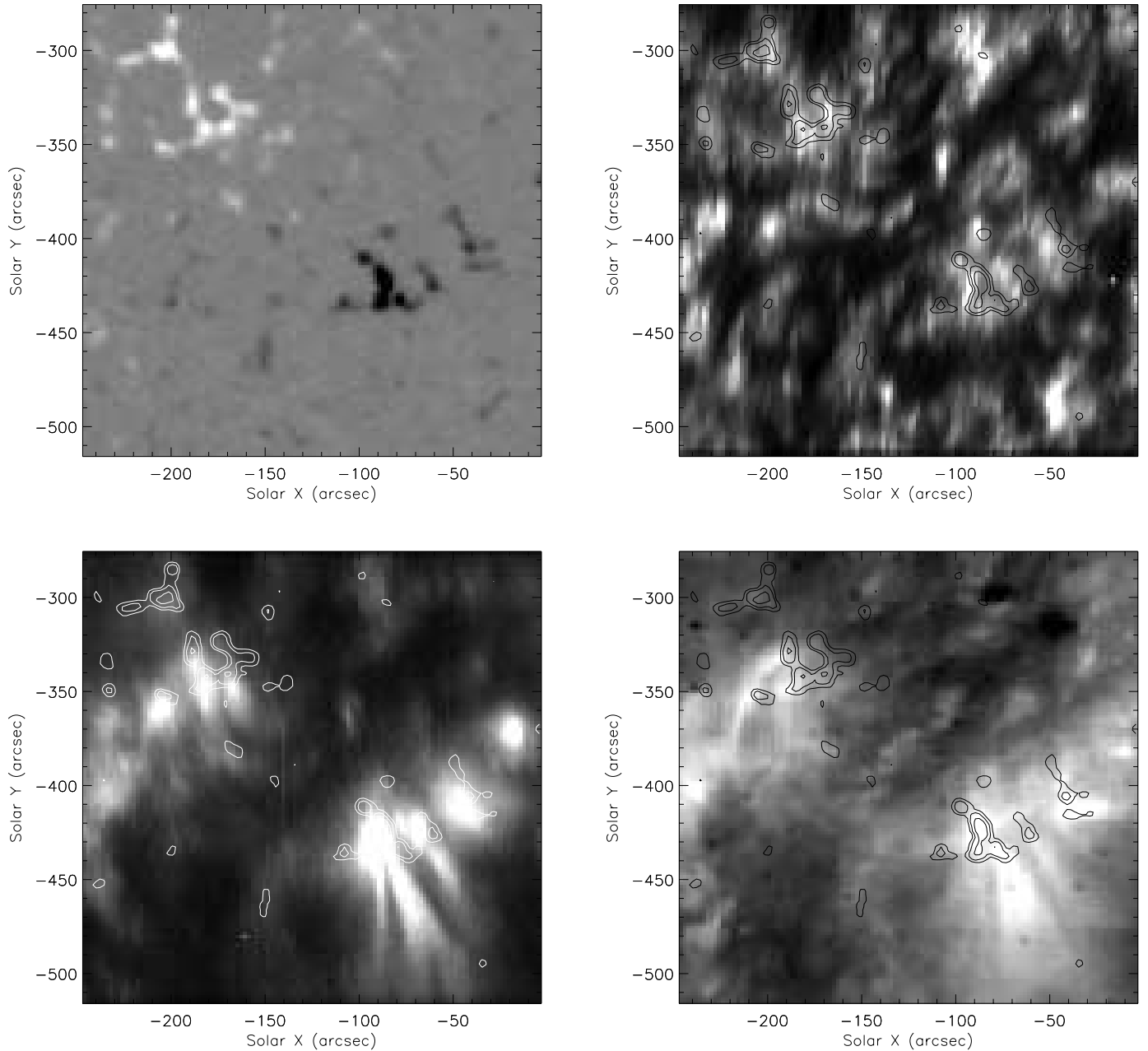


FIG. 1.—Magnetic field from MDI (*top left*; white is positive polarity, black is negative polarity), O  $v$   $\lambda 629.73$  CDS intensity map (*top right*;  $3 \times 10^5$  K), Mg ix  $\lambda 368.07$  CDS intensity map (*bottom left*;  $10^6$  K), and EIT  $\lambda 171$  intensity map (*bottom right*;  $1.3 \times 10^6$  K). Magnetic field contours from MDI are superimposed on all maps.

of the results. Agreement between temperature measurements from the two techniques confirms the robustness of the loop selection and of the background subtraction.

Once the plasma electron density was known, the expected EM for each subsection was calculated, assuming that the loop cross section  $S$  is circular, measuring its radius from CDS monochromatic images, and using the subsection length  $L$ . Comparison between the predicted and measured EM values can provide the plasma filling factor  $ff$ , given by

$$ff = \frac{EM_{\text{obs}}}{EM_{\text{pred}}}, \quad EM = N_e^2 SL. \quad (23)$$

Line-of-sight speed measurements were made from line shifts, assuming that they are caused by Doppler effects.

Plasma velocities can be determined by considering the geometry of the observed loop.

#### 4.1. The Emission Measure Analysis

The concepts of EM and DEM were first introduced by Pottasch (1963) and have been reviewed and further discussed by Mariska (1992) and Mason & Monsignori Fossi (1994). A method for the determination of the EM in isothermal plasmas and its application to CDS and SUMER spectra on *SOHO* can be found in Landi et al. (2002) and is briefly summarized below. The flux of an optically thin line emitted by an isothermal plasma and observed at distance  $d$  can be written as

$$F_i = \frac{1}{4\pi d^2} G_i(T_c, N_e) \langle EM \rangle, \quad \langle EM \rangle = \int_V N_e^2 dV, \quad (24)$$

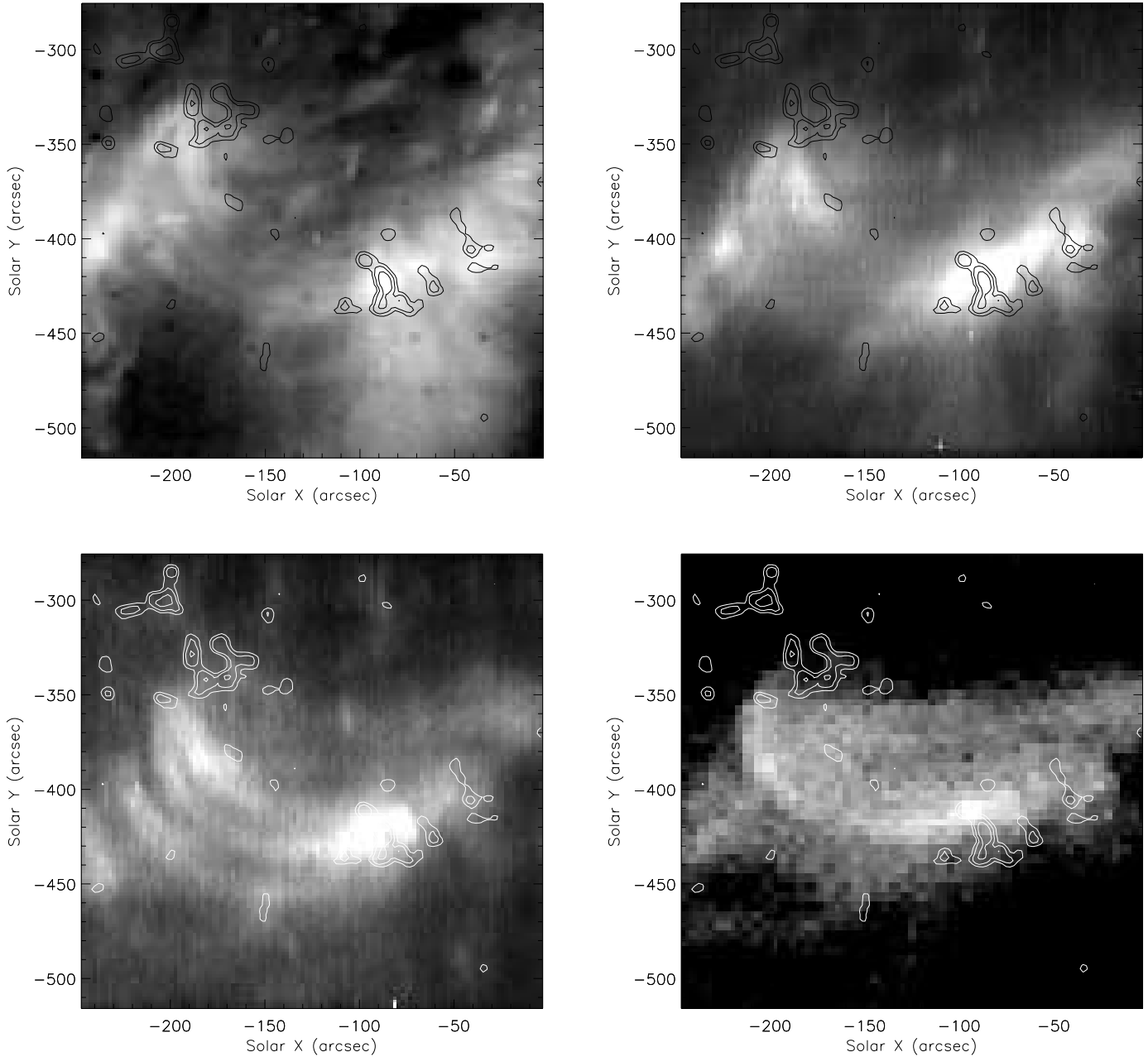


FIG. 2.—EIT  $\lambda 195$  intensity map (top left;  $1.6 \times 10^6$  K), Si xii  $\lambda 520.67$  CDS intensity map (top right;  $1.9 \times 10^6$  K), Fe xvi  $\lambda 360.76$  CDS intensity map (bottom left;  $3 \times 10^6$  K), and Yohkoh SXT intensity map (bottom right;  $T \geq 2 \times 10^6$  K). Magnetic field contours from MDI are superimposed to all maps.

where  $N_e$  and  $T_c$  are the plasma electron density and temperature, respectively,  $V$  is the emitting volume along the line of sight,  $G_i(T, N_e)$  is the contribution function of the emitting line, usually dependent on both electron temperature and density, and  $\langle \text{EM} \rangle$  is the emission measure of the plasma. The diagnostic method consists of calculating the function  $\langle \text{EM}(T) \rangle$  defined as

$$\langle \text{EM}^i(T) \rangle = 4\pi d^2 \frac{F_{\text{obs}}^i}{G_i(T, N_e)} \quad (25)$$

as a function of the electron temperature  $T$ , using the observed fluxes  $F_{\text{obs}}^i$  of each observed CDS line  $i$  and the electron density value derived from line ratio techniques. When all the  $\langle \text{EM}(T) \rangle$  curves are displayed in the same plot as a function

of temperature, these curves should intersect at a common point  $(T_c, \langle \text{EM} \rangle)$  if the plasma is isothermal. Given the experimental uncertainties, this will define a narrow range in the  $T_c$ - $\langle \text{EM} \rangle$  space. The crossing point and its uncertainties are determined as the region where the largest number of the  $\langle \text{EM}(T) \rangle$  curves meet. Examples can be found in Figure 6 (see later for discussion).

In the present work, the atomic data in the CHIANTI database were used to calculate relative level populations. Ion fractions from Mazzotta et al. (1998) and the element abundances of Feldman & Laming (2000) are used to derive the contribution function of each observed line. The Feldman & Laming (2000) photospheric abundances of the elements whose first ionization potential (FIP) is lower than 10 eV were increased by a factor of 3.5 to yield coronal abundances, as indicated by Feldman et al. (1999) and Landi et al. (2002).

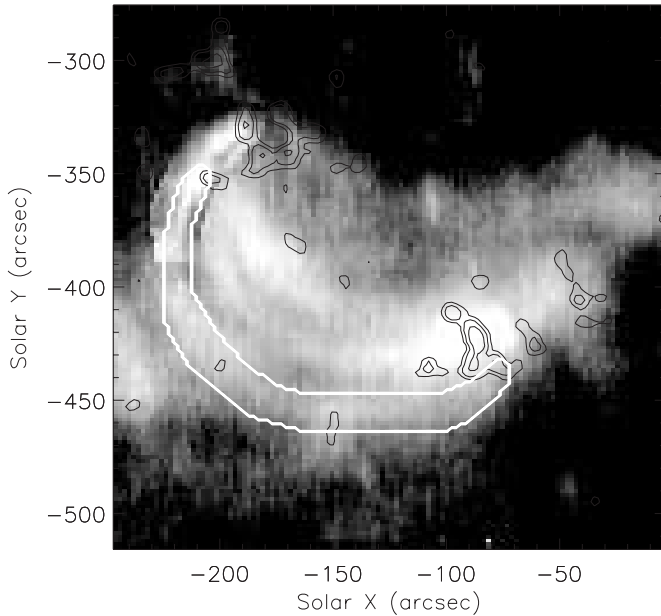


FIG. 3.—Composite intensity map obtained with CDS in the Fe xvi  $\lambda 360.76$  line and the EIT  $\lambda 171$  channel. The shape of the selected loop is overplotted. Magnetic field contours from MDI have also been displayed to show the loop footpoints. The EIT emission has been used to show the position of the left footpoint of the selected loop and is visible as a result of the different background intensity. The position of the right footpoint is rather uncertain.

#### 4.2. Diagnostic Results

Measured electron densities are displayed in the top panel of Figure 7: the density is approximately constant within the error bars, although uncertainties are quite high. There is some indication that the electron density might be increasing at the loop top, but the amount of increase is comparable to the uncertainties themselves.

Results from the EM analysis are displayed in Figures 6 and 7 (*bottom panel*). In the EM analysis, the Si xii  $\lambda 520.6$  line has been discarded because of atomic physics problems (Landi et al. 2002), while the Fe xii  $\lambda 364.4$  line has been used only when it had significant background-subtracted intensity. Figure 6 displays the  $\langle EM(T) \rangle$  functions for all the lines in a sample of subsections. The ions contributing to Figure 6 are Fe xii (where available), Fe xiii, Fe xiv, Fe xvi, and Si xi. Their temperatures of maximum ion abundance range between 1.5 and 4 million degrees. Figure 6 shows that for all subsections (except for the top left one) it is possible to determine a common crossing point from which the electron temperature and the EM can be determined. The existence of such a common crossing point also indicates that the plasma along the line of sight is isothermal within uncertainties and hence that the loop plasma in each subsection has uniform temperature. This result is further discussed in § 5.6. The top left panel, on the contrary, does not provide a common crossing point. This subsection corresponds to the left footpoint of the loop, and its non-isothermality is due to the fact that the line of sight encompasses the whole temperature gradient of the loop from the corona to the chromosphere, so that non-isothermality is expected. All the subsections not reported in Figure 6 show the same behavior of the isothermal subsections, with the only exception of the one corresponding to the right footpoint, which behaves in the same way as the top left panel in Figure 6.

The EM profile of the selected loop is displayed in the bottom panel of Figure 7, and it is approximately constant within uncertainties.

The loop temperature profile is shown in Figure 8. The individual measurements and their error bars correspond to the temperature measurements obtained with the EM analysis. Each individual curve corresponds to the temperature measurements obtained from line ratios from lines emitted by different stages of ionization of Fe (Fe xii, Fe xiii, Fe xiv, Fe xvi). With the only exception of one curve, all the line ratios agree with the temperature profile determined by the EM analysis. The temperature curve that shows disagreement involves an Fe xii line, whose flux is highly uncertain as a result of the background subtraction, as shown by Figure 4. Figure 8 shows that (1) the loop temperature profile is constant, confirming earlier spectroscopic results in Paper I and from imagers (Neupert et al. 1998; Aschwanden et al. 1999; Lenz et al. 1999), and (2) temperature diagnostics from CDS background-subtracted spectra yield self-consistent and robust results.

The brightening that occurred at 3–40,000 km seems to be only a small perturbation to the overall structure: it causes an increase in EM and temperature within the uncertainties and no change in electron density.

The measured temperature and EM values have been used to predict the count rates expected in the three EIT coronal channels (EIT  $\lambda 171$ , EIT  $\lambda 195$ , and EIT  $\lambda 284$ ) and in *Yohkoh* SXT, using the standard EIT and SXT software. Comparison between estimated and observed count rates provides a check on the robustness of the present diagnostic results; this is especially important for EIT  $\lambda 171$  and *Yohkoh* SXT, since they are mostly sensitive to temperatures different from the measured values. Figure 9 shows the comparison between the predicted and observed count rates for the three coronal channels of EIT. Counts rates are usually quite low, and this explains the high uncertainties. In Figure 9, dashed lines represent the predicted count rates, while the solid line with error bars represents the observed count rates. Uncertainties are given by the sum of uncertainties in both observed and predicted count rates; the latter are due to the errors in the measurements in the plasma EM and temperature. Agreement within uncertainties between predicted and estimated count rates in all channels is shown in Figure 9. Footpoints are not reported, since the plasma is not isothermal and observed count rates in the EIT  $\lambda 171$  and EIT  $\lambda 195$  channels far exceed those predicted using the plasma EM and temperature values from the rest of the loop, as expected. Predicted and observed count rates for SXT are both negligible; however, when an additional high-temperature component at 3 or 4 MK is added, SXT count rates rise to nonnegligible levels, thus exceeding the observed ones. Such high-temperature components have smaller effects on the predicted EIT count rates, since EIT channels are sensitive to lower temperatures. The agreement between predicted and observed count rates for EIT and SXT confirms the CDS-based diagnostic results.

Measurement of line centroids along the loop has shown that line-of-sight speeds are negligible along the whole profile of the loop. Given the strong inclination of the loop relative to the line of sight, plasma velocities from Doppler shifts can be greatly underestimated. However, the absence of motions at the footpoints, where the loop axis should be more aligned to the line of sight, suggests that plasma motions are negligible along the whole structure.

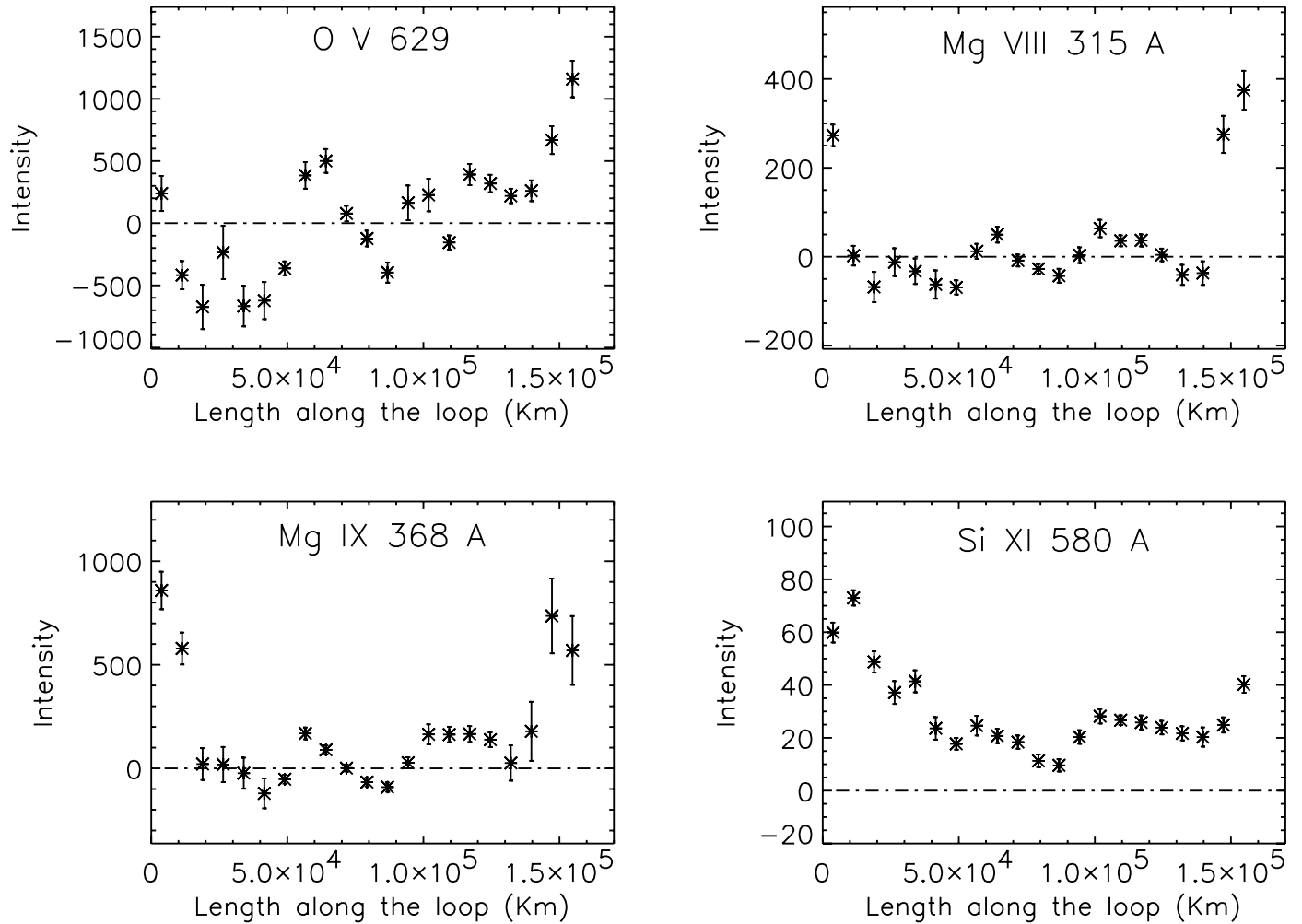


FIG. 4.—Intensity of several observed lines as a function of position along the loop, after background subtraction. Intensities are in  $\text{ergs cm}^{-2} \text{s}^{-1} \text{sr}^{-1}$ .

The plasma pressure can be calculated from the temperature and density profiles and is constant within the experimental uncertainties, confirming the fact that the maximum height above the photosphere reached by the loop is lower than the loop plasma scale height and that the whole structure is strongly inclined from the radial direction. The constant pressure value is  $0.9 \pm 0.2 \text{ dynes cm}^{-2}$ .

From the EM and density measurements it is possible to determine the plasma filling factor for each subsection. The volume  $V$  occupied by each subsection can be calculated by approximating each subsection to a cylinder with circular cross section. The length of this cylinder is given by the length of the subsection ( $\approx 7150 \text{ km}$ ), and the radius of its subsection has been taken from Paper I to be  $4300 \pm 1100 \text{ km}$ . The resulting filling factors are in the 0.1–1.0 range; their values, however, are only rough estimates because of uncertainties in the electron density and in the radius of the loop cross section. Higher spatial resolution and instrument throughput are needed to improve the accuracy of the filling factor estimates.

##### 5. COMPARISON WITH THE THEORETICAL MODEL

The comparison between model predictions and observations has been carried out using the observed and theoretical density and temperature profiles. The uncertainty in the velocity profile has prevented its comparison with predicted velocities.

As input, we have used the plasma pressure  $p_0 = 0.9 \pm 0.2 \text{ dynes cm}^{-2}$  measured by CDS and the total loop length of the loop  $L_{\text{loop}} = 150,000 \pm 15,000 \text{ km}$ , obtained from CDS monochromatic images after correction for the loop geometry. The inclination of the loop plane from the vertical has been assumed to be  $80^\circ$ , in agreement with Paper I. Theoretical profiles have been calculated by assuming three different heating functions  $H(z)$ : uniform heating, exponential heating concentrated at the footpoints, and exponential heating concentrated at the loop top. In the case of exponential heating, we have varied its scale height  $H_0$ .

By varying the parameters  $a$  and  $F_0$ , we have investigated the effects on the resulting temperature and density profiles of the presence of plasma velocity and of nonnegligible conductive flux at the footpoints. The chosen values are  $F_0 = 0, -10^6, -5 \times 10^6, -10^7 \text{ ergs cm}^{-2} \text{ s}^{-1}$  and  $a = 0, 10^{-31}, 10^{-30}, 10^{-29}$ . The real velocities corresponding to these values of  $a$  depend on the loop model and typically range from 0 ( $a = 0$ ) to  $70 \text{ km s}^{-1}$  ( $a = 10^{-29}$ ).

This approach allows us to explore the parameter space of the theoretical model, in search of a possible combination of heating function, velocities, and footpoint conductive flux that allows us to reproduce the observations.

The experimental uncertainties in the loop pressure, total length, and inclination angle have also been explored. This allows us to assess the importance of uncertainties in the

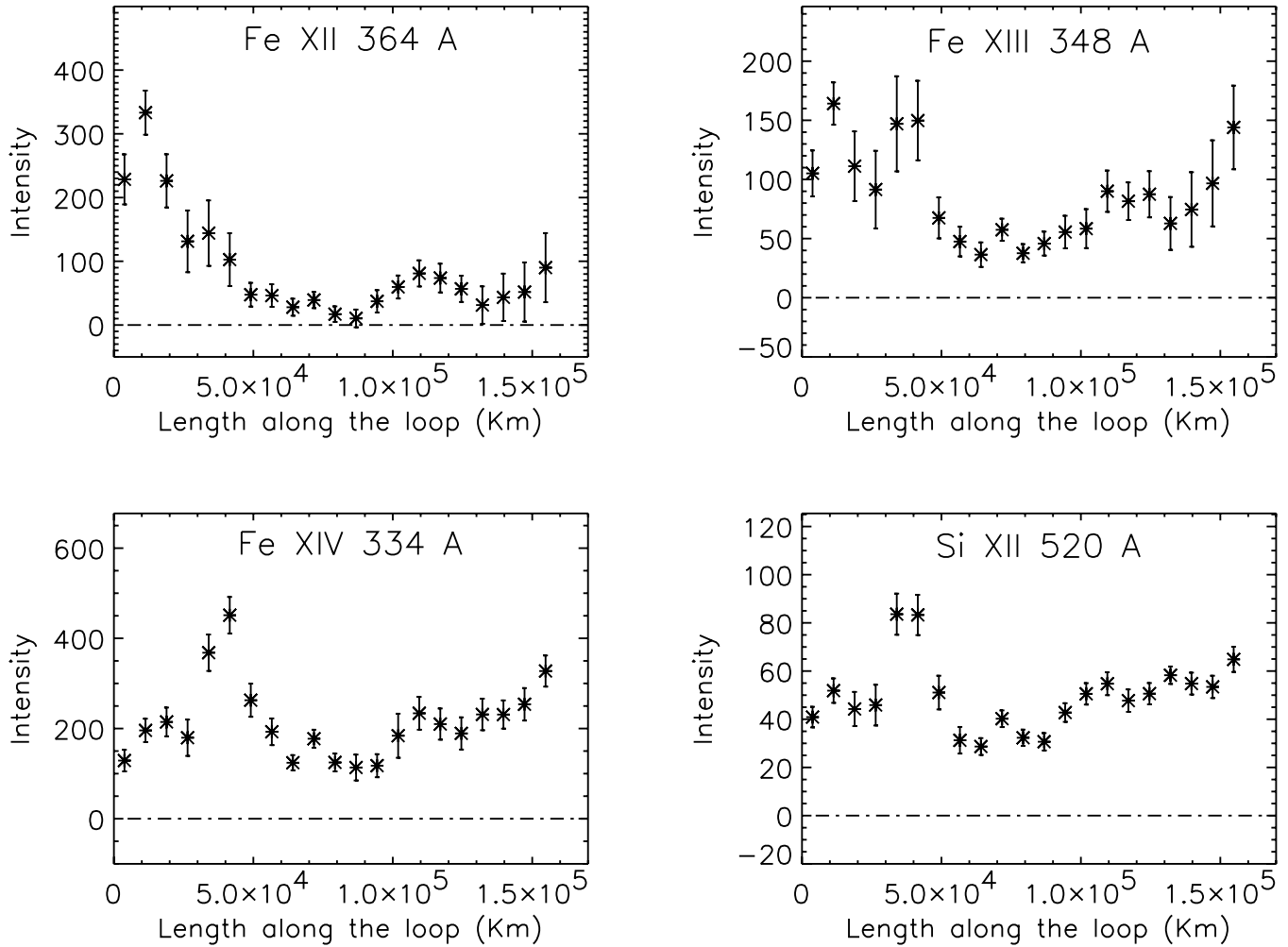


FIG. 4.—Continued

loop pressure and loop geometry as defined by CDS. It is anticipated that spectrometers with greater spatial resolution and higher throughput will reduce the effects discussed here. The effect of using a different set of element abundances (namely, coronal or photospheric) also allows us to assess the effect of uncertainties in plasma composition on loop studies.

5.1. Uniform Heating

Figure 10 reports the comparison between observations and predictions obtained with a uniform heating. The electron density profile shows some underestimation of the density at loop center; the electron temperature is in all cases higher than observed by a factor of 1.5–2, and its profile is much less isothermal than suggested by CDS, with a smooth gradient toward the footpoints. The presence of velocity introduces an asymmetry in the temperature and density profiles.

The presence of nonzero velocities and conductive flux at the footpoints has the effect of raising the loop top temperature and increasing the disagreement with the observations. Figure 10 shows that uniform heating is inadequate to reproduce plasma diagnostic results. Such inadequacy was already noted by several authors.

5.2. Exponential Heating—Top

Figure 11 reports the comparison between observations and model predictions obtained with exponential heating concentrated at the loop top, described as

$$E_i(\theta) = E_0^i e^{-[(\theta - \pi/2)/b]^2}, \quad b = \frac{H_0}{R_{loop}}. \quad (26)$$

The parameter  $H_0$  controls the concentration of the heating at the loop top: large values of  $H_0$  (i.e.,  $\geq 50,000$  km) approach the uniform heating results. Small values of  $H_0$  cause the temperature and density profiles to be less constant at the loop top, indicating a larger temperature peak and a deeper electron density minimum than in the uniform heating case.  $H_0$  has been varied down to 10,000 km, but the smaller its value, the more pronounced are the temperature peak and the density minimum. The presence of velocity and conductive flux at the footpoints increases the temperature and decreases the density, and velocities also introduce asymmetry in the profiles.

Figure 11 clearly shows that the disagreement with observations is even larger than in the uniform heating case, and it becomes worse in the case of more concentrated heating. The results thus show that top heating is inadequate to reproduce the observations.

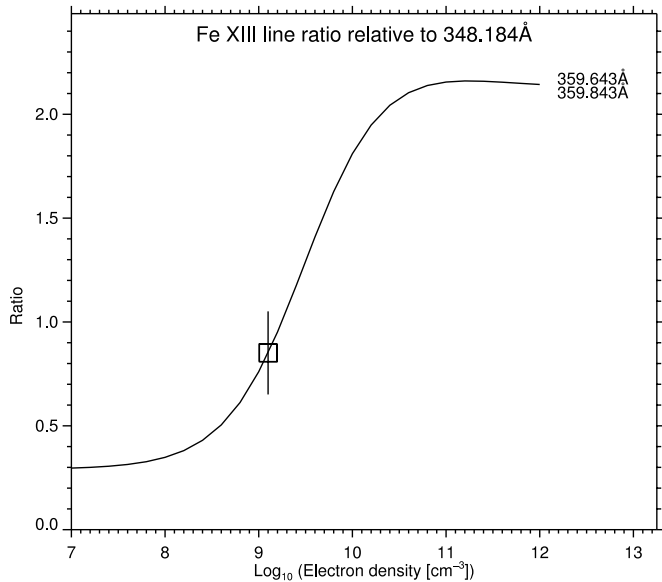


FIG. 5.—Line intensity ratio between the Fe XIII  $\lambda\lambda(359.643+359.843)/\lambda 348.184$  lines. The line ratio is calculated in energy units.

### 5.3. Exponential Heating—Footpoints

Figure 12 reports the comparison between observations and model predictions obtained with exponential heating concentrated at the loop footpoints, described as

$$E_i(\theta) = E_0^i \frac{e^{-\theta/b} + e^{-(\pi-\theta)/b}}{2b(1 - e^{-\pi/b})}, \quad b = \frac{H_0}{R_{\text{loop}}}. \quad (27)$$

Large values of  $H_0$  approach the uniform heating limit. Unlike the other two heating functions investigated, low values of  $H_0$  may cause the model to produce unphysical solutions, or no solution at all. For example, in the case with  $a = 0$  and  $F_0 = 0$ , the height  $H_0 = 45,000$  km produces solutions with symmetric profiles and a correct temperature of  $T = 10^4$  K at the right footpoint. Lower values of  $H_0$  produce temperature profiles with a minimum at the loop top, which corresponds to a maximum in density: such condensation at loop top would make the loop dynamically unstable. For even lower values of  $H_0$ , the model is unable to converge to  $T = 10^4$  K at the right footpoint, so no solution is possible. The minimum value of  $H_0$  for which it is still possible to obtain a physical solution depends on the value of  $F_0$ . For  $F_0 = -10^6$  ergs  $\text{cm}^{-2} \text{s}^{-1}$ , the minimum  $H_0$  is 35,000 km; for  $F_0 = -5 \times 10^6$  ergs  $\text{cm}^{-2} \text{s}^{-1}$ , the minimum  $H_0$  decreases to 20,000 km; and for  $F_0 = -10^7$  ergs  $\text{cm}^{-2} \text{s}^{-1}$ , the minimum  $H_0$  reaches 15,000 km. The value of  $a$  does not have a significant effect on the minimum  $H_0$  for which solutions are possible.

Lower values of  $H_0$  produce more constant temperature and density profiles, bringing them in closer agreement with observations; the presence of velocities introduces asymmetries to the profiles.

Figure 12 shows that although the temperature profile is flatter and closer to observations than with the previous heatings, no agreement can be found. Predicted temperatures are still too high, and the presence of nonzero velocities and conductive flux at the footpoints only increases the value of the top temperature. Predicted densities are slightly lower than observed.

In summary, exponential heating at the footpoints is not able to reproduce the observed quantities in the loop considered in the present work.

### 5.4. Effects of Uncertainties in the Loop Length, Pressure, and Inclination Angle

The effect of the inclination angle on the temperature and density profiles is not sufficient to account for the discrepancies we find. Even selecting  $\alpha = 0$  (loop plane perpendicular to the solar surface), thus maximizing the effects of gravity, the temperature profile does not change its shape and its top temperature decreases only by a few percent in all cases.

The effects of plasma pressure are more important. Although the shape of the temperature profile is not changed, lower pressure values provide lower top temperatures: the difference is at maximum 10% adopting the smallest possible value of  $p_0 = 0.7$  dynes  $\text{cm}^{-2}$ . Higher pressures increase the top temperature by similar amounts. These changes, although significant, are not sufficient to achieve agreement.

Longer loops are characterized by higher top temperatures, while shorter loops are cooler. However, even using the two extremes of the loop length uncertainties, the changes in the top temperature do not exceed 4%. No change occurs in the temperature profiles. Therefore, even though the location of the right footpoint of the selected loop is not well determined, its uncertainty is not sufficient to affect the results of the present comparison.

### 5.5. Effects of Different Element Abundances

The radiative losses depend critically on the set of elemental abundances adopted to calculate them. As shown by Landi & Landini (1999), large variations, as high as a factor of 2 or more, can occur on the radiative losses following a different choice of the element abundances. Cook et al. (1989) also discussed the significant consequences of such changes on loop models. In principle, the disagreement between the theoretical model and the observations found in the previous sections could be solved by a different set of abundances.

In order to check whether our results change if we use a different set of abundances, we have repeated the comparison described in the previous sections using the photospheric set of abundances of Grevesse & Sauval (1998). The difference between this set and the coronal abundances used in the previous sections consists of a decrease by a factor of  $\simeq 4$  of the abundances of the elements with FIP smaller than 10 eV. This difference has small effect at transition region temperatures, since the emission is mostly due to oxygen and carbon, and is most important at coronal temperatures, dominated by the emission from elements with  $\text{FIP} \leq 10$  eV.

Figure 13 shows the comparison between the model-based and the measured electron temperature. In the top panel the heating was uniform (*dashed line*) and concentrated at the top (*solid line*), with  $a = F_0 = 0$ ; in the bottom panel the heating was concentrated at the footpoints, with variable  $H_0$  and  $F_0$  and  $a = 0$ . The parameter  $a$  was not varied since its effect is only to introduce asymmetry and raise the top temperature;  $F_0$  was varied in the footpoint-heated case to investigate heating functions strongly concentrated at the footpoint (down to 15,000 km).

In all cases, Figure 13 shows that the change in coronal composition does not alter qualitatively the results: the theoretical model is unable to reproduce the observed temperature

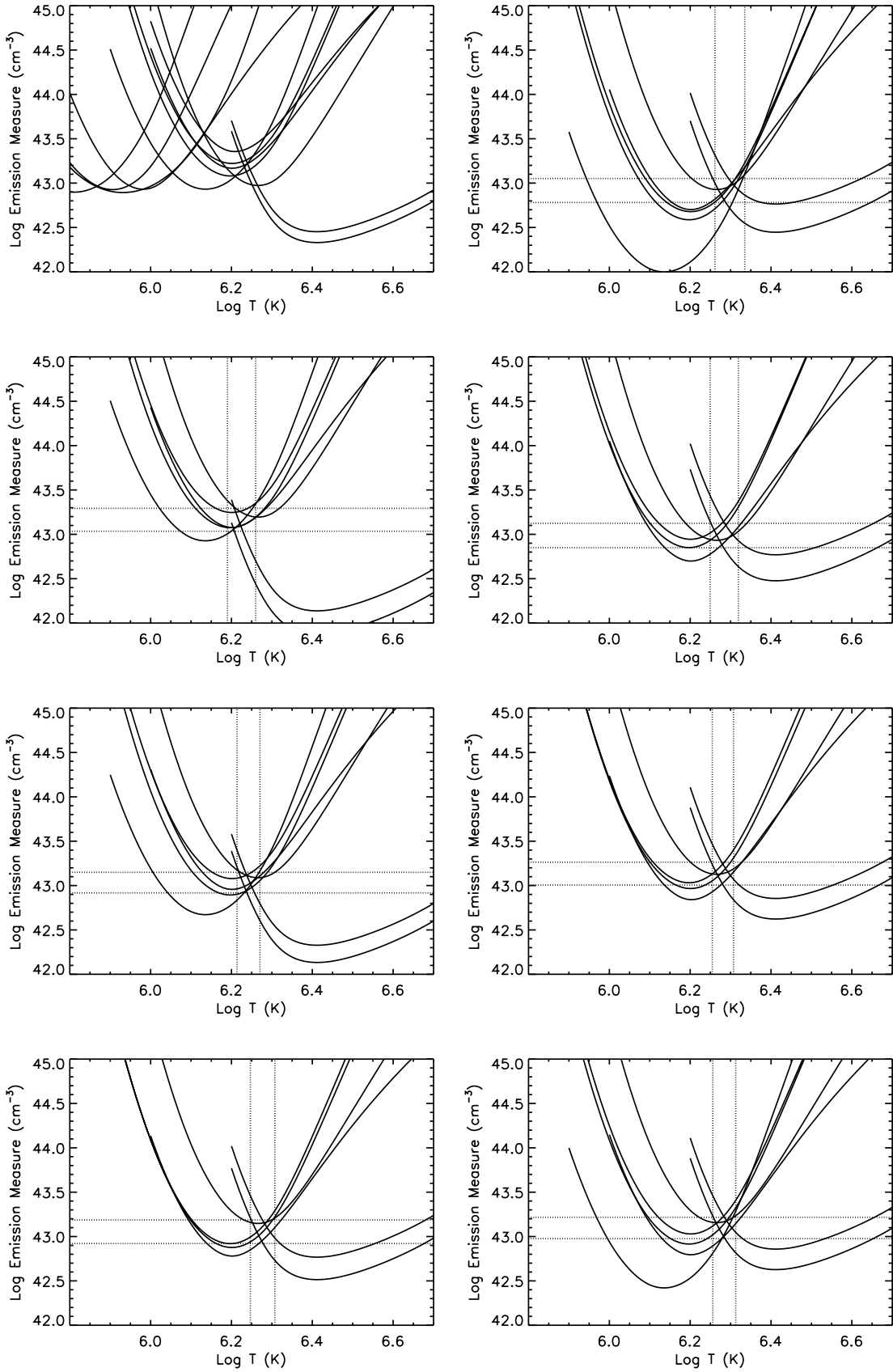


FIG. 6.—EM diagnostics for selected subsections of the loop. The top left panel corresponds to the left footpoint of the selected loop, while the other panels correspond to subsections in the middle of the loop. Average subsection fluxes have been used.

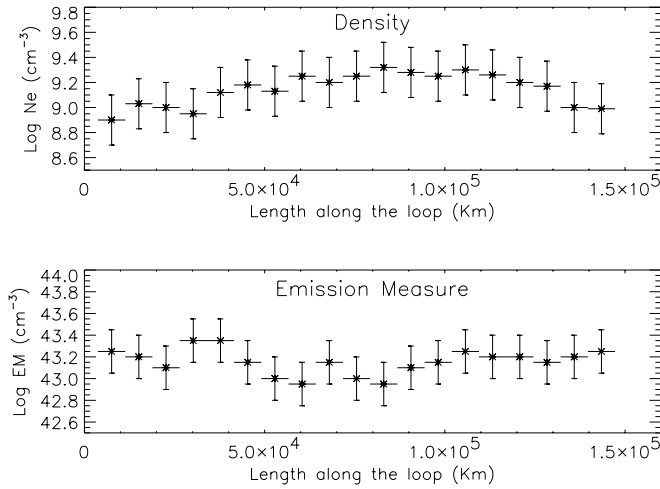


FIG. 7.—Measured density and average EM as a function of position along the selected loop.

profile, predicting too high temperatures and a non-isothermal temperature profile. However, the effect of lower abundances is to decrease the top temperature, although the change is not sufficient to achieve agreement.

Fludra & Schmelz (1999) suggested another set of coronal abundances using flare data, which require high-FIP abundances decreased by a factor of 1.5 and low-FIP abundances increased by a factor of 2.1 relative to photospheric values. We have also investigated the changes in the model predicted temperature profiles brought by this set of abundances and found that they cause a decrease in the top temperature of  $\approx 8\%$  and no change in the temperature profile, so that the discrepancy between the model and observations is still unsolved.

### 5.6. Effects of Limitations in Available Spectral Lines

The present result that the loop plasma is isothermal also along the line of sight is of great importance for models (see § 5.7), but it needs to be discussed in light of the limitations of the present observations. In fact, the five ions whose intensity survived the background subtraction and that were used in the EM analysis were mainly formed in the  $(1.5-4) \times 10^6$  K range. However, they are not very sensitive to any plasma

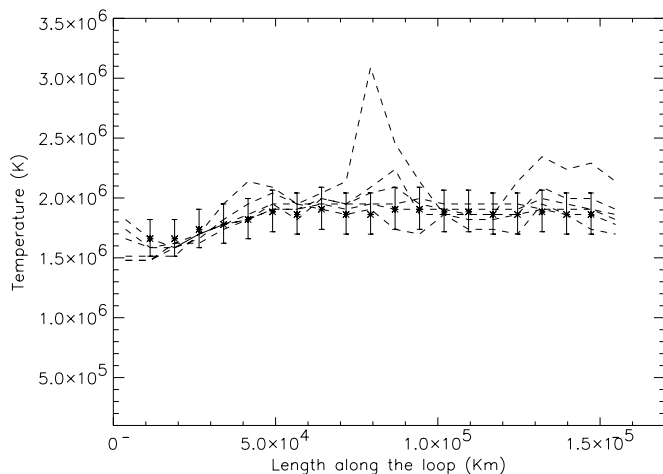


FIG. 8.—Temperature measurements along the selected loop. *Crosses*: EM analysis results; *dashed curves*: results from line ratios.

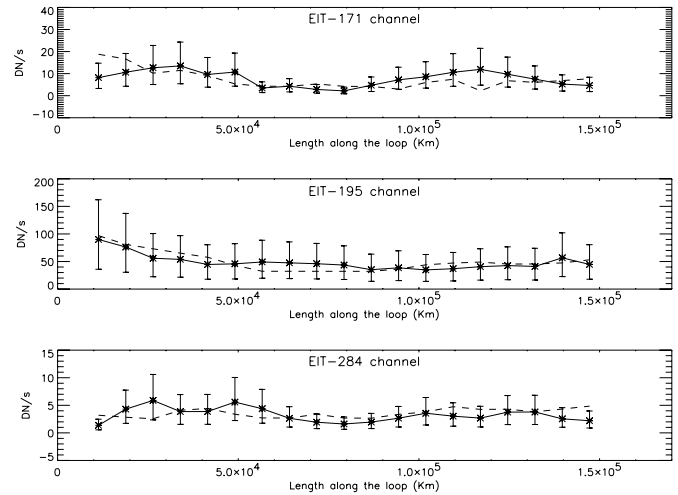


FIG. 9.—Observed (*solid line and crosses with error bars*) and predicted (*dashed lines*) count rates along the selected loop for the three EIT coronal channels. Error bars combine uncertainties in observed count rates from EIT images in predicted count rates. Footpoints are not reported.

outside this temperature range, so that additional hotter or colder plasma components give no signature in this data set. In addition, the absence of lines formed at temperatures outside the  $(1.5-4) \times 10^6$  K range can limit the sensitivity of the EM analysis itself to plasma components with temperatures in the  $(3-4) \times 10^6$  K range. We have investigated this by carrying out the EM analysis over a simulated data set that includes the spectral lines used in the present work, whose contribution functions are calculated with a two-temperatures plasma model: one temperature is the one measured in the present work, while the second temperature is  $3 \times 10^6$  K ( $\log T = 6.5$ ); the same EM value has been assigned to both components. Using the CHIANTI database, we have calculated the expected intensities of the lines used in § 4, and we applied the EM analysis on this simulated data set. Results show that a crossing point can still be defined, although with larger uncertainties and more confused EM- $T$  curves than those in Figure 6. A similar result is found when the second component is at  $T = 4 \times 10^6$  K. We did not investigate low-temperature components, since the weakness of the strong Mg IX  $\lambda 368.1$  present in our data set indicates that no significant plasma at  $10^6$  K is present in the loop plasma. This result, however, clearly demonstrates that the lack of ions formed at temperatures higher than  $4 \times 10^6$  K in the present data set limits the accuracy of the EM analysis beyond the measured flux uncertainties, so that CDS alone is not able to provide a definitive proof that the loop plasma is isothermal along the line of sight. Unfortunately, telemetry and cadence constraints, as well as the CDS wavelength range, prevented us from observing lines from ions formed outside the  $(1.5-4) \times 10^6$  K range (i.e., Si IX, Fe X, Fe XI, Fe XII, Fe XIII). Their absence in our data sets therefore greatly limits the reliability of the EM results.

However, the availability of EIT and *Yohkoh* data allows us to greatly restrict the range of loop plasma temperature. In fact, predicted *Yohkoh* SXT count rates substantially rise if plasma with a temperature of  $(3-4) \times 10^6$  K is present along the line of sight, exceeding the observed count rates. In the same way, additional low-temperature (i.e.,  $T \approx 10^6$  K) plasma would cause a large increase in EIT  $\lambda 171$  expected count rates, exceeding observations (as well as a large enhancement

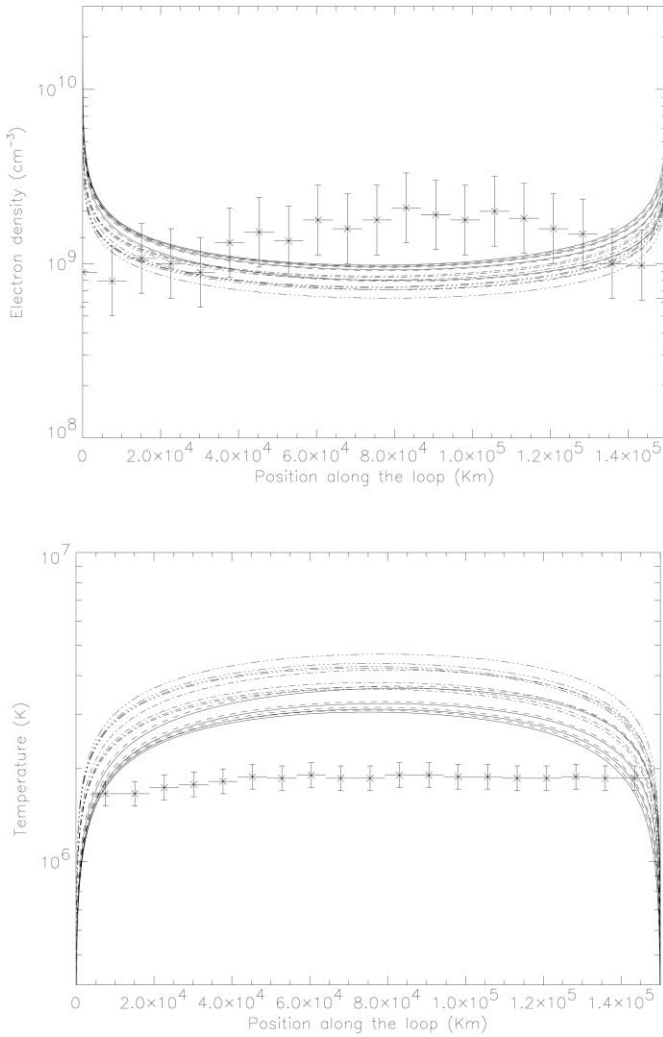


FIG. 10.—CDS diagnostic results and theoretical predictions based on a uniform heating model, with varying  $F_0$  and  $a$ . *Top*: Comparison between the predicted and measured electron densities. *Bottom*: Comparison between the predicted and measured electron temperatures.

of the Mg IX line flux). Therefore, EIT and *Yohkoh* count rates provide support to the results of the EM analysis carried out with CDS line intensities. This analysis also shows that broadband imagers, especially in the X-ray range, can provide very important contributions when combined with high-resolution spectrometers.

In summary, spectroscopically resolved EUV observations are a powerful tool to probe the loop plasma isothermality, but the present CDS observations require the help of EIT and SXT data to provide conclusive results. The small number of lines in the present data set was driven by (1) limitations in the selection of ions whose lines fall in the CDS wavelength range and (2) limitations in exposure time for each slit position in the raster, so that the signal-to-noise ratio of many lines was too low to survive the background subtraction. These limitations offer compelling evidence of the need of new spectrometers with high throughput, fast cadence, and wide temperature coverage and ion selection.

### 5.7. Discussion

The failure of the proposed heating functions to reproduce the observed loop profiles opens the question of alternative approaches to achieve agreement.

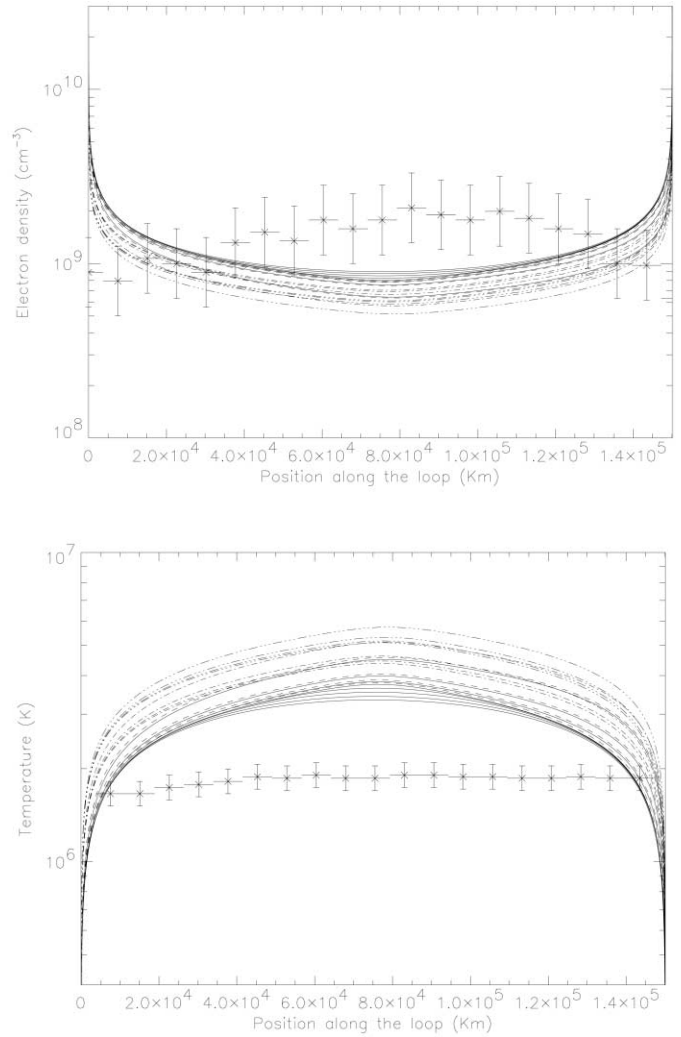


FIG. 11.—CDS diagnostic results and theoretical predictions based on an exponential heating concentrated at the top, with varying  $F_0$ ,  $a$ , and  $H_0$ . *Top*: Comparison between the predicted and measured electron densities. *Bottom*: Comparison between the predicted and measured electron temperatures.

An improvement to the model that might have beneficial impacts on the comparison with observations is a variable loop cross section. As noted in Paper I, while the coronal section of the loop seemed to have an approximately constant cross section, it was difficult to trace it down to transition region or chromospheric temperatures. They proposed a variable loop cross section parameterized as a function of temperature and used observations to constrain it. The presence of a variable cross section would imply a smaller EM at the loop footpoint and would alter the energy equation. Future studies will be devoted to this issue.

The presence of filamentation, suggested by the measured filling factor and also by high-resolution, narrowband imagers such as EIT and *TRACE*, does not seem to be an obvious solution in the presence of steady heating. In fact, in case all filaments are identical, the present analysis still applies to each filament and hence to the overall structure, so that agreement cannot be found. In case the unresolved filaments have different temperatures, the loop structure resulting from the superposition of independent strands at different temperatures would be multithermal across the line of sight, contrary to the scenario suggested by the present results.

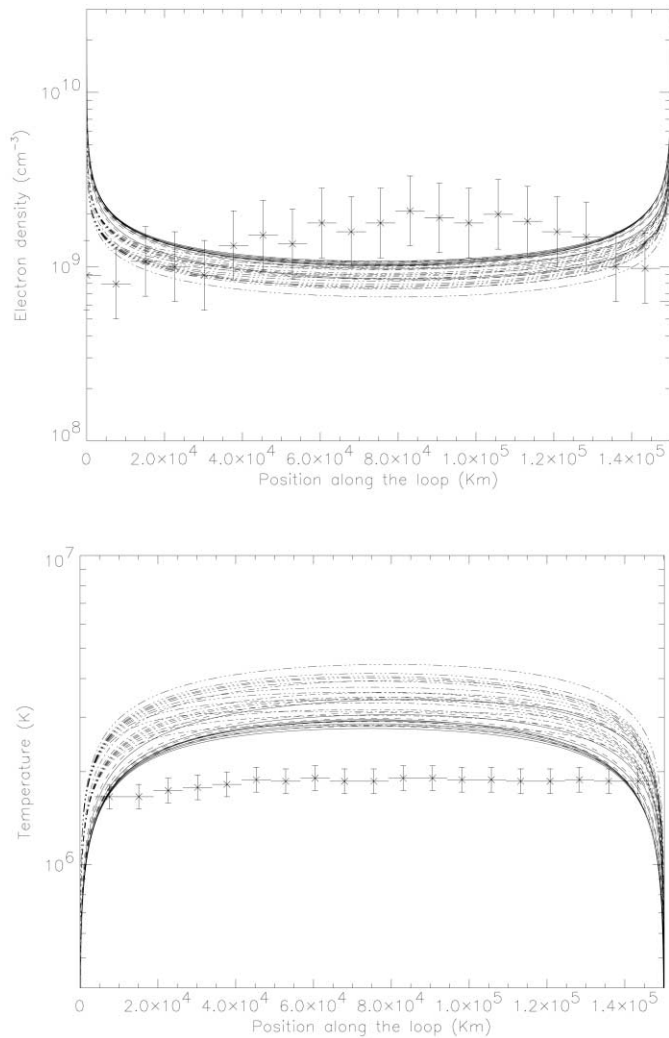


FIG. 12.—CDS diagnostic results and theoretical predictions based on an exponential heating concentrated at the footpoints, with varying  $F_0$ ,  $a$ , and  $H_0$ . *Top*: Comparison between the predicted and measured electron densities. *Bottom*: Comparison between the predicted and measured electron temperatures.

Another possibility is given by the presence of nonsteady heating, which causes each individual strand to be cooling down after impulsive heating. However, the presence of different strands at different stages of their cooling within the instrument's resolution element would cause the plasma to be multithermal, contrary to our diagnostic results. An escape from this situation might be the presence of nonequilibrium conditions in each strand's plasma. Such a situation would invalidate the assumptions under which the plasma emissivity and radiative losses have been calculated and might mimic an isothermal, equilibrium situation. Under nonequilibrium conditions model predictions would be different, since the radiative loss curve might change significantly. A model dealing with nonequilibrium cooling loop models in a self-consistent way has been recently developed by Bradshaw & Mason (2003) but is unavailable to us. A future paper will be devoted to developing such a model and to comparing its predictions with the present observations.

## 6. SUMMARY AND CONCLUSIONS

In the present work, CDS, EIT, and *Yohkoh* observations of a quiescent active region loop have been analyzed to (1) measure the main loop physical quantities and (2) compare

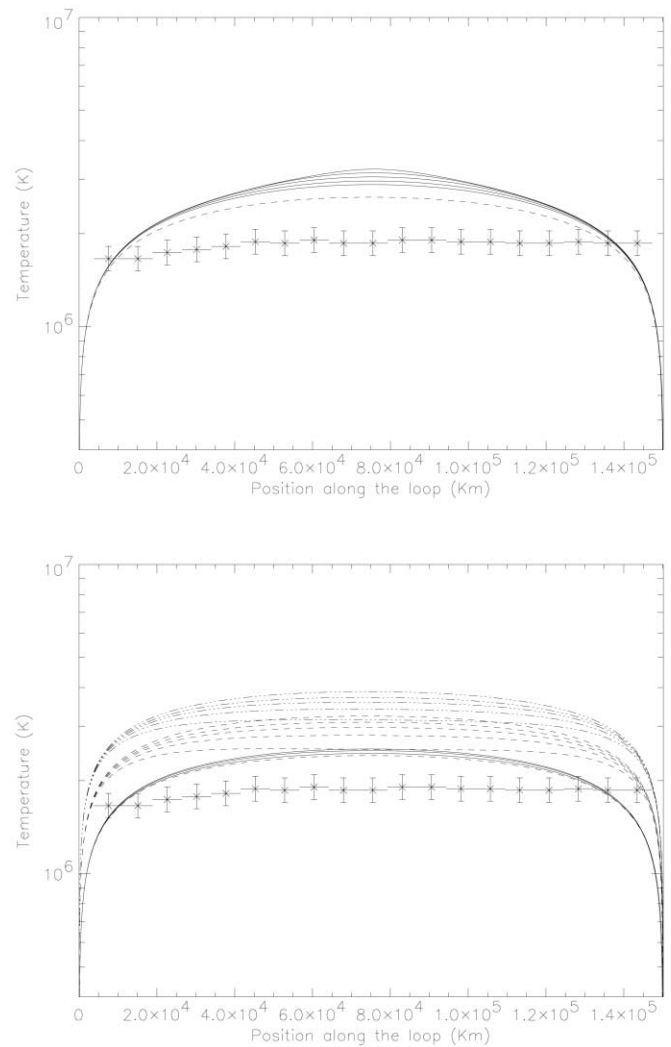


FIG. 13.—CDS diagnostic results and theoretical predictions. *Top*: Uniform (dashed line) and exponential heating concentrated at the loop top (solid line);  $a = F_0 = 0$  in all cases. *Bottom*: Heating concentrated at the footpoints, with varying  $F_0$  and  $H_0$  and  $a = 0$ . Solid line:  $F_0 = 0$ ; dashed line:  $F_0 = -5 \times 10^6$  ergs  $\text{cm}^{-2} \text{s}^{-1}$ ; dot-dashed line:  $F_0 = -1 \times 10^7$  ergs  $\text{cm}^{-2} \text{s}^{-1}$ .

the diagnostic results with a one-dimensional, steady state, dynamic loop model, assuming three different heating functions: uniform, concentrated at the loop top, and concentrated at the loop footpoints.

Plasma diagnostic results show the following:

1. The loop is isothermal along its main axis for nearly all its length.
2. Electron temperature is approximately constant across the loop cross section.
3. Temperatures measured with two different techniques show excellent agreement.
4. The loop EM along the loop is constant within uncertainties.
5. The loop filling factor is in the 0.1–1.0 range, possibly implying that the loop is constituted by unresolved filaments.

The comparison of model predictions with the diagnostic results has shown the following:

1. The model produces density profiles in broad agreement with observations in all cases, although the uncertainties in the density are high and discrepancies are found in some cases.

2. Uniform and exponential heating concentrated at the top is not able to reproduce the observed temperature: the temperature profiles are not uniform as observed, and the loop top temperature is too high in all cases.

3. Exponential heating concentrated at the footpoints produces more uniform temperature profiles, but the top temperature is still too high.

4. The scale height  $H_0$  of the exponential heating concentrated at the footpoints needs to be chosen carefully, as below a minimum scale height the model produces either nonphysical solutions or no solution at all.

5. The value of this minimum scale height depends on the conductive flux at the footpoint  $F_0$ : greater  $F_0$  allow smaller  $H_0$  values.

6. The uncertainties in the observed input parameters, namely, loop total length, loop pressure at the footpoints, and loop plane inclination relative to the solar surface, have some effects on the predicted loop top temperature, but not in its profile. These effects are too small to account for the difference between our model and observations.

7. Using photospheric abundances in place of coronal values decreases the loop temperature but is not able to achieve agreement.

The possible scenarios that might allow us to obtain agreement between loop models and observations are also discussed.

The present work demonstrates that even with their inadequate spatial resolution, existing spectrometers are able to provide meaningful plasma diagnostics and significant insight into loop physics. In particular, we have shown that it is possible to minimize the effects of contamination of the loop emission from nearby structures not properly resolved by the

instrument; furthermore, we have shown that the effects of the residual uncertainties in the loop shape selection and in the input parameters affect only moderately the diagnostic results and the comparison with the model predictions. However, CDS observations alone are not able to provide definitive evidence of isothermality in the selected loop's plasma because of cadence and temperature coverage limitations, and only with the help of data from EIT and *Yohkoh* can we draw solid conclusions about the loop isothermality.

The limiting factors to current spectrometers, i.e., low spatial resolution and cadence, can be overcome with improved technologies and optical design that enhance throughput and resolution. Such improvements will enable observers to produce spectrally resolved, monochromatic imaging of large portions of the Sun. On the contrary, the limitations affecting narrowband imagers, i.e., low temperature resolution and inability of measuring densities, filling factors, and line-of-sight velocities, are intrinsic to such instruments and very difficult to be solved by technological advances. Therefore, it is highly recommended that in future space missions spectrometers be included.

Future spectroscopic instruments such as *Solar-B* EIS, to be launched in 2006, will have a much higher spatial resolution than CDS, and it is expected that significant advances in loop physics will result from the analysis of EIS data.

We warmly thank the referee for valuable comments that helped to improve the present work. *SOHO* is a mission of international cooperation between ESA and NASA. The work of E. L. was supported under the Living with a Star Target Research and Technology program.

#### REFERENCES

- Aschwanden, M. J. 2001, *ApJ*, 559, L171  
 Aschwanden, M. J., et al. 1999, *ApJ*, 515, 842  
 ———. 2000, *ApJ*, 531, 1129  
 Binello, A. M., Landi, E., Mason, H. E., Storey, P. J., & Brosius, J. W. 2001, *A&A*, 370, 1071  
 Bradshaw, S. J., & Mason, H. E. 2003, *A&A*, 401, 699  
 Brković, A., Landi, E., Landini, M., Ruedi, I., & Solanki, S. 2002, *A&A*, 383, 661 (Paper I)  
 Cargill, P. J., & Klimchuk, J. A. 1997, *ApJ*, 478, 799  
 Chae, J., Park, Y. D., Moon, Y.-J., Wang, H., & Yun, H. S. 2002, *ApJ*, 567, L159  
 Cook, J. W., Cheng, C.-C., Jacobs, V. L., & Antiochos, S. K. 1989, *ApJ*, 338, 1176  
 Delaboudinière, J.-P., et al. 1995, *Sol. Phys.*, 162, 291  
 Dere, K. P., Landi, E., Mason, H. E., Monsignori Fossi, B. C., & Young, P. R. 1997, *A&AS*, 125, 149  
 Di Giorgio, S., Reale, F., & Peres, G. 2003, *A&A*, 406, 323  
 Feldman, U., Doschek, G. A., Schuhle, U., & Wilhelm, K. 1999, *ApJ*, 518, 500  
 Feldman, U., & Laming, M. J. 2000, *Phys. Scr.*, 61, 222  
 Fludra, A., & Schmelz, J. T. 1999, *A&A*, 348, 286  
 Grevesse, N., & Sauval, A. J. 1998, *Space Sci. Rev.*, 85, 161  
 Harrison, R. A., et al. 1995, *Sol. Phys.*, 162, 233  
 Klimchuk, J. A., & Porter, L. J. 1995, *Nature*, 377, 131  
 Landi, E., Feldman, U., & Dere, K. P. 2002, *ApJS*, 139, 281  
 Landi, E., & Landini, M. 1999, *A&A*, 347, 401  
 Landini, M., & Monsignori Fossi, B. C. 1981, *A&A*, 102, 391 (LM81)  
 Lenz, D. D., et al. 1999, *ApJ*, 517, L155  
 Mariska, J. T. 1992, *The Solar Transition Region* (Cambridge Astroph. Ser. 23; Cambridge: Cambridge Univ. Press)  
 Martens, P. C. H., Cirtain, J. W., & Schmelz, J. T. 2002, *ApJ*, 577, L115  
 Mason, H. E., & Monsignori Fossi, B. C. 1994, *A&A Rev.*, 6, 123  
 Mazzotta, P., Mazzitelli, G., Colafrancesco, S., & Vittorio, N. 1998, *A&AS*, 133, 403  
 Neupert, W. N., et al. 1998, *Sol. Phys.*, 183, 305  
 Pottasch, S. R. 1963, *ApJ*, 137, 945  
 Priest, E. R. 1982, *Solar Magnetohydrodynamics* (Dordrecht: Riedel)  
 Priest, E. R., et al. 1998, *Nature*, 393, 545  
 ———. 2000, *ApJ*, 539, 1002  
 Reale, F. 2002, *ApJ*, 580, 566  
 Reale, F., & Peres, G. 2000, *ApJ*, 528, L45  
 Rosner, R., Tucker, W. H., & Vaiana, G. S. 1978, *ApJ*, 220, 643  
 Scherrer, P. H., et al. 1995, *Sol. Phys.*, 162, 129  
 Schmelz, J. T. 2002, *ApJ*, 578, L161  
 Schmelz, J. T., Scopes, R. T., Cirtain, J. W., Winter, H. D., & Allen, J. D. 2001, *ApJ*, 556, 896  
 Spitzer, L. 1962, *Physics of Fully Ionized Gases* (New York: Wiley)  
 Testa, P., Peres, G., Reale, F., & Orlando, S. 2002, *ApJ*, 580, 1159  
 Tsuneta, S., et al. 1991, *Sol. Phys.*, 136, 37  
 Warren, H. P., Winebarger, A. R., & Hamilton, P. S. 2002, *ApJ*, 579, L41  
 Winebarger, A. R., Warren, H. P., & Mariska, J. T. 2003, *ApJ*, 587, 439  
 Winebarger, A. R., Warren, H. P., van Ballegooijen, A., De Luca, E. E., & Golub, L. 2002, *ApJ*, 567, L89  
 Young, P. R., Del Zanna, G., Landi, E., Dere, K. P., Mason, H. E., & Landini, M. 2003, *ApJS*, 144, 135